K. Elkhodary
Department of Mechanical and Aerospace Engineering,
North Carolina State University,
2412 Broughton Hall,
Box 7910,
Raleigh, NC 27695-7910

Lipeng Sun

Douglas L. Irving

Donald W. Brenner

Department of Materials Science and Engineering,
North Carolina State University,
Raleigh,
NC 27587-7907

G. Ravichandran
Graduate Aeronautical Laboratories,
California Institute of Technology, Aeronautics and Mechanical Engineering,
Mail Stop 105-50,
Pasadena, CA 91125

M. A. Zikry
Department of Mechanical and Aerospace Engineering,
North Carolina State University,
2412 Broughton Hall,
Box 7910,
Raleigh, NC 27695-7910

Integrated Experimental, Atomistic, and Microstructurally Based Finite Element Investigation of the Dynamic Compressive Behavior of 2139 Aluminum

The objective of this study was to identify the microstructural mechanisms related to the high strength and ductile behavior of 2139-Al, and how dynamic conditions would affect the overall behavior of this alloy. Three interrelated approaches, which span a spectrum of spatial and temporal scales, were used: (i) The mechanical response was obtained using the split Hopkinson pressure bar, for strain-rates ranging from 1.0×10^{-3} s to 1.0×10^{4} s^{-1}. (ii) First principles density functional theory calculations were undertaken to characterize the structure of the interface and to better understand the role played by Ag in promoting the formation of the Ω phase for several Ω-Al interface structures. (iii) A specialized microstructurally based finite element analysis and a dislocation-density based multiple-slip formulation that accounts for an explicit crystallographic and morphological representation of Ω and θ' precipitates and their rational orientation relations were conducted. The predictions from the microstructural finite element model indicated that the precipitates continue to harden and also act as physical barriers that impede the matrix from forming large connected zones of intense plastic strain. As the microstructural FE predictions indicated, and consistent with the experimental observations, the combined effects of θ' and Ω, acting on different crystallographic orientations, enhance the strength and ductility, and reduce the susceptibility of 2139-Al to shear strain localization due to dynamic compressive loads. [DOI: 10.1115/1.3129769]

1 Introduction

High strength Al–Cu–Mg alloys, such as 2024-Al and 2048-Al, were widely used in applications that require high fracture toughness and crack propagation resistance, such as aircraft structures, automotive applications, armored vehicles, and electronic packaging devices. These alloys do not generally perform well at high temperatures. Therefore, heat resistant alloys, such as 2219-Al and 2618-Al, were used in applications that require high specific strength and high temperature capability. These heat resistant Al–Cu–Mg alloys, however, have limited fracture strength and damage tolerance [1].

The addition of small amounts of Ag to Al–Cu–Mg alloys with high Cu to Mg ratios can significantly improve the age hardening response by the nucleation of thermally stable, platelike Ω precipitates on {111} planes in the aluminum matrix [2]. Moreover, Al–Cu–Mg–Ag alloys have less grain boundary (GB) precipitation, and therefore retain most of their toughness after age hardening, and were less susceptible to intergranular fracture [3,4].

Therefore, Al–Cu–Mg–Ag alloys can potentially have relatively high strength, temperature resistance, toughness, and damage tolerance. Specifically, the Al–Cu–Mg–Ag alloy 2139-T8 developed by Cho and Bes [5] showed, after the addition of Mn for dispersoid formation, significantly improved fatigue life and fracture toughness in comparison to currently used alloys in the aerospace industry. Moreover, the ballistic performance of 2139-Al was also shown to be potentially superior to that of Al-2519, which is used in armored vehicles [5].

The potential use of Al–Cu–Mg–Ag alloys for different applications was therefore predicated on understanding, identifying, and optimizing the material mechanisms and behavior related to increased strength and toughness. If these alloys were to be tailored for a desired application, optimal trade-offs between the competing requirements of strength and toughness have to be identified and controlled. Hence, a detailed understanding of the microstructural constituents in 2139-Al and their influence on the mechanical behavior is needed. Specifically, it has to be understood why the addition of Ag was favorable to the formation of Ω precipitates, how Ω and θ' precipitates affect toughening and strengthening behavior at different scales in terms of microstructural characteristics, such as crystal orientation and dislocation-density interactions at matrix-precipitate interfaces. A comprehensive experimental-cum-modeling overview of these issues was lacking, especially for high strain-rate modes and regimes.

Hence, the objective of this study was to identify the microstructural mechanisms related to the high strength and ductile behavior of 2139-Al, and how dynamic conditions would affect the overall response of this alloy. Hence, three interrelated approaches were used: (i) The mechanical response (stress-strain) behavior was obtained using the split Hopkinson (Kolsky) pressure bar, for

Contributed by the Applied Mechanics Division of ASME for publication in the JOURNAL OF APPLIED MECHANISM. Manuscript received June 5, 2008; final manuscript received December 29, 2008; published online June 15, 2009. Review conducted by Ashkan Vaziri.

strain-rates ranging from 1.0×10^{-3} s to 1.0×10^{4} s^{-1}. (ii) First principles density functional theory calculations were conducted to characterize the structure of the interface and to better understand the role played by Ag in promoting the formation of the Ω phase for several Ω-Al interface structures. (iii) A specialized microstructurally based finite element (FE) analysis and dislocation-density based multiple-slip formulation that accounts for an explicit representation of precipitates and their rational orientation relations was conducted. This microstructural formulation accounted for precipitate shape, aspect ratio, volume fraction, crystal structure, and the different slip systems and orientations associated with the alloy matrix and precipitates. The effects of stress and plastic slip accumulation at precipitate interfaces, GBs, grain interiors, and dislocation-density evolution at the matrix-precipitate interfaces were investigated. This integrated approach provided insights that are difficult, if not impossible to obtain, if only an experimental or a computational approach was used.

This paper is organized as follows: An overview of the experimental method was presented in Sec. 1, the first principles results are given in Sec. 2, an outline of the microstructural approach and specialized FE approach are given in Sec. 3, the results are discussed in Sec. 4, and a summary of the salient conclusions are given in Sec. 5.

2 High Strain-Rate Experiments

The high strain-rate behavior of metals and alloys was widely recognized to play an important role in several technologies including manufacturing processes, such as rolling, forming, and high-speed machining, as well as in ballistic failure, dynamic crack growth, and shear banding. Accurate computational modeling of these processes requires the knowledge of material behavior at large strains over a wide range of strain rates. Relevant constitutive data were also essential for validating and developing multiscale material models [6,7]. The validation of such models requires robust experimental measurements that can be used to aid in the refinement of these models aimed at bridging length scales in high strain-rate deformation of metals. The dynamic nature of the above mentioned processes motivated the study of high-strain rate deformations.

In this section a description of the large strain mechanical response of 2139-Al over strain rates ranging from $\dot{\varepsilon}\approx10^{-3}-10^{4}$ s^{-1} is presented. The material of this study was supplied as rolled plates from Alcan Rolled Products (Ravenswood, WV) and then machined as cylinders.

Quasistatic testing was carried out on a computer controlled MTS servohydraulic machine, operated under displacement control. The machine's stiffness was taken into account when producing stress-strain data. High-rate constitutive behavior was investigated using a 19 mm diameter Kolsky (split Hopkinson) pressure bar [8], made of C300 maraging steel. The signal processing accounted for wave dispersion according to the algorithm of Lifshitz and Leber [9]. Strain-rate jump tests were carried out using specially designed 30 cm long cylindrical projectiles. Two cylindrical impactors were used. The geometry of the first had a length of 15 cm where the diameter is constant at 19 mm, and for the remainder of the 30 cm length, the diameter was stepwise reduced from 19 mm to 12.7 mm. The second impactor also had a constant diameter of 19 mm along the first 15 cm of length, and for the remainder of the impactor length, the diameter was also stepwise reduced from 19 mm to 9.61 mm. The specimens were cylindrical, with 6 mm in diameter and 6 mm in length.

Typical stress-strain curves obtained over a wide range of strain rates are shown in Fig. 1. At quasistatic strain rates ($\sim10^{-3}$ s^{-1}), the material exhibited considerable hardening; it deformed to large equivalent strains of up to 10% and had a strength of approximately 800 MPa, which is significantly higher than most aluminum alloys. As the strain rate was increased to 8100/s, the material exhibited significant ductility of up to 80%. There was slight stress softening, but as seen from Fig. 1, the strengths were only slightly lower than those observed in the quasistatic regime. The strain-hardening behavior did not seem to be highly rate dependent. The stress-strain response softened in the dynamic regime at true strains below 10%. The flow stress at $\varepsilon_{true}=0.06$ is plotted as a function of strain rate in Fig. 2. The material exhibited considerable rate sensitivity, particularly at strain rates beyond 10^{3} s^{-1}. The highest strain rate achieved was approximately 10^{4} s^{-1}, a strain rate that was generally not achievable in a split Hopkinson (Kolsky) pressure bar using cylindrical specimens. These results were an indication of 2139-Al's high strength and significant ductility over a span of different strain rates. Atomistic and microstructurally based FEM modelings were used to further understand the underlying mechanisms that affect this response.

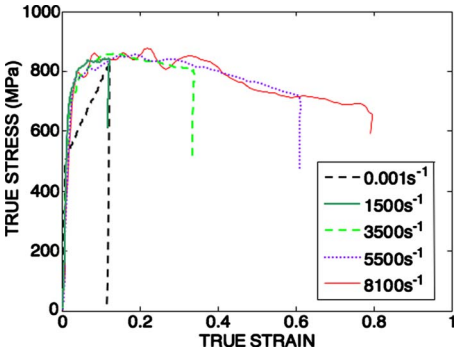

Fig. 1 True-stress true-strain curves for 2139-Al under varied loading rates. The quasistatic stress-strain curve, obtained from the MTS servohydraulic machine under displacement control, shows considerable hardening. The high strain-rate curves, obtained from the split Hopkinson pressure bar, show extensive ductility (up to 80%) and slight stress softening of the 2139-Al alloy.

3 Atomistic Modeling of Omega Precipitates

To characterize the structure of the interface and to better understand the role played by Ag in promoting the formation of the Ω phase, which could be one of the main microstructural characteristics affecting the desirable behavior of 2139-Al, first principles density functional theory calculations were carried out on several Ω-Al interface structures both with and without Ag and Mg. The calculations used the Vienna ab initio simulation package (VASP) [10,11], and were carried out within the generalized gradient approximation using the PW91 parameterization [12,13]. Valence-core electron interactions were treated using ultrasoft pseudopotentials [14], and the valence electron wave functions were expanded in plane wave basis sets with a 300 eV energy cutoff using the Monkhorst–Pack method for special *k*-point sam-

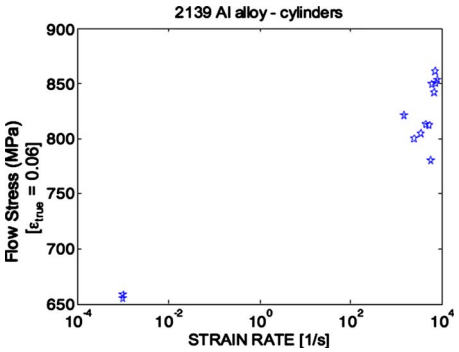

Fig. 2 Strain-rate sensitivity of flow stress in 2139-Al at an equivalent strain of 0.06 exhibiting considerable material rate sensitivity, particularly at strain rates beyond 10^{3} s^{-1}

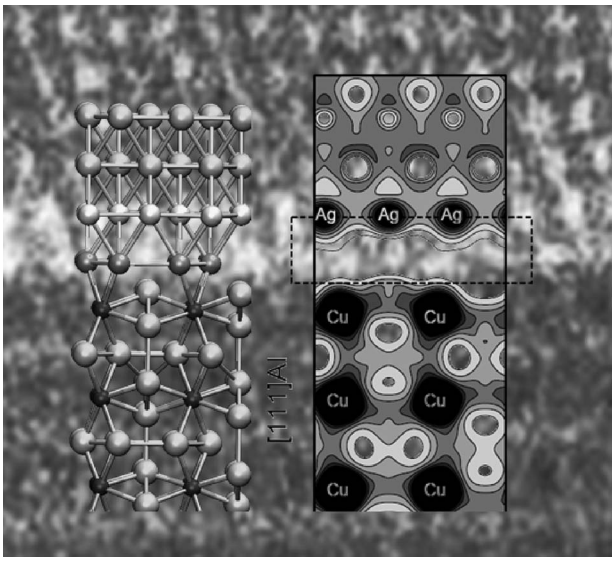

Fig. 3 Superposition of the atomic arrangement (left) and the electron density (right) from the first principles calculations over the experimental *Z* contrast HRTEM image from Ref. [1] of the Al-Ω interface

pling for the Brillouin zone integration [15]. Three-dimensional periodic boundary conditions were applied, and both the cell volume and atomic positions within the cell were relaxed.

A small supercell of 76 atoms was used to characterize the pure α-Al/Ω interfacial structure. Three different types of chemical bonds, Al–Al, Al–Cu, or Al–Cu plus Al–Al may be formed across the α-Al/Ω interface depending on the termination of the (001) Ω planes. Several relative displacements of the Ω structure, with respect to the Al lattice, were used as initial structures within these three termination types followed by energy minimization. The most stable structure of the α-Al/Ω interface was found to be connected by Al–Al bonds with a hexagonal Al lattice on the surface of the Ω phase, sitting on the vacant hollow sites of the Al {111} matrix plane.

Starting with this interface structure, heats of formation were calculated for an extensive set of trial structures in which Mg and/or Ag atoms were substituted for the interfacial Al. A larger 152 atom supercell was used for these calculations to reduce size effects and supercell image interactions. The results of these calculations indicate that when only Mg is introduced, the tendency for segregation to the interface was minimal and the strength of the interface was not enhanced. In contrast, Ag has a strong tendency to segregate to a dense substitutional layer that was one layer away from the interface into the Al lattice. This occurs because Ag and Al form relatively strong bonds, and there was a reduced planar density of Al atoms in the Ω phase to which the Ag can bond. However, the strongest bonding, and hence the greatest stabilization of the interface, occurs when the Mg substitutes for the Al layer closest to Ω phase and the Ag substitutes for the Al in the next layer into the Al, hence forming an interfacial bilayer like that observed experimentally. To illustrate the relationship of structure to experiment, shown in Fig. 3 is a superposition of the atomic arrangement (left) and the electron density (right) from the first principle calculations over the experimental *Z* contrast high resolution transmission electron microscopy (HRTEM) image from Ref. [16] of the Al-Ω interface. Our theoretically determined structure allows strong Ag–Al, Mg–Cu, and Ag–Mg bonding while excluding the weaker Ag–Cu bonds. The analysis of the charge density at the interface shows a net transfer of electrons to the Ω and Al matrix from the interface region that contributes to interface stabilization. Hence, the first principle modeling provides both a viable atom-resolved structure consistent with experiment and provides insight into the driving force for the stability of this interface in terms of bonding strengths and electron charge transfer.

4 Microstructural Finite Element Model

4.1 Crystal Plasticity Formulation. Constitutive formulations for the rate-dependent multiple-slip crystal plasticity, which are coupled to the evolutionary equations for the dislocation densities, were used. For a detailed presentation, see Refs. [17–19].

The velocity gradient was decomposed into a symmetric deformation rate tensor D_{ij} and an antisymmetric spin tensor W_{ij}. D_{ij} and W_{ij} were then additively decomposed into elastic and plastic components as

$$D_{ij} = D_{ij}^{*} + D_{ij}^{p} \tag{1a}$$

$$W_{ij} = W_{ij}^{*} + W_{ij}^{p} \tag{1b}$$

The inelastic parts are defined in terms of the crystallographic slip rates as

$$D_{ij}^{p} = P_{ij}^{(\alpha)} \dot{\gamma}^{(\alpha)} \tag{2a}$$

$$W_{ij}^{p} = \omega_{ij}^{(\alpha)} \dot{\gamma}^{(\alpha)} \tag{2b}$$

where α is summed over all slip systems, and $P_{ij}^{(\alpha)}$ and $\omega_{ij}^{(\alpha)}$ are the symmetric and antisymmetric parts of the Schmid tensor in the current configuration, respectively.

The rate-dependent constitutive description on each slip system can be characterized by a power law relation, for strain rates below a critical value of $\dot{\gamma}_{\text{critical}}$ as

$$\dot{\gamma}^{(\alpha)} = \dot{\gamma}_{\text{ref}}^{(\alpha)} \left[\frac{\tau^{(\alpha)}}{\tau_{\text{ref}}^{(\alpha)}} \right] \left[\frac{|\tau^{(\alpha)}|}{\tau_{\text{ref}}^{(\alpha)}} \right]^{1/m-1} \tag{3}$$

where $\dot{\gamma}_{\text{ref}}^{(\alpha)}$ is the reference shear strain rate, which corresponds to a reference shear stress $\tau_{\text{ref}}^{(\alpha)}$, and m is the rate sensitivity parameter. Above the critical strain rate $\dot{\gamma}_{\text{critical}}$, where the phonon drag is assumed to dominate, m is taken as 1 and $\dot{\gamma}_{\text{ref}}^{(\alpha)} = \dot{\gamma}_{\text{critical}}$. Mughrabi [20] stressed that what was used here was a modification of widely used classical forms that relate the reference stress to a square-root dependence on the dislocation density (ρ_{im}) as

$$\tau_{\text{ref}}^{(\alpha)} = \left(\tau_{y}^{(\alpha)} + G \sum_{\rho=1}^{\text{nss}} a_{\rho} B^{(\rho)} \sqrt{\rho_{im}^{(\rho)}} \right) \left(\frac{T}{T_0} \right)^{-\xi} \tag{4}$$

where $\tau_{y}^{(\alpha)}$ is the static yield stress on slip system (α), G is the shear modulus, nss is the number of slip systems, $B^{(\rho)}$ is the magnitude of the Burgers vector, and the coefficients a_{ρ} are the slip-system interaction coefficients. T is the temperature, T_0 is the reference temperature, and ξ is the thermal softening exponent.

For a given deformed state of the material, the dislocation structure of total dislocation density $\rho^{(\alpha)}$ is additively decomposed into a mobile and an immobile dislocation density $\rho_{m}^{(\alpha)}$ and $\rho_{im}^{(\alpha)}$, respectively, as

$$\rho^{(\alpha)} = \rho_{m}^{(\alpha)} + \rho_{im}^{(\alpha)} \tag{5}$$

It is assumed that during an increment of strain, there ensues a change in the dislocation structure. The balance between generation and annihilation of dislocation densities as a function of strain is thus taken as a basis for the following equations that describe the evolution of mobile and immobile dislocation densities:

$$\frac{d\rho_{m}^{(\alpha)}}{dt} = |\dot{\gamma}^{(\alpha)}| \left[\frac{g_{\text{sour}}}{B^{(\alpha)} B^{(\alpha)}} \left(\frac{\rho_{im}^{(\alpha)}}{\rho_{m}^{(\alpha)}} \right) - \frac{g_{\text{minter}}}{B^{(\alpha)} B^{(\alpha)}} \exp\left(- \frac{\Delta H}{kT} \right) - \frac{g_{\text{immob}}}{B^{(\alpha)}} \sqrt{\rho_{im}^{(\alpha)}} \right] \tag{6}$$

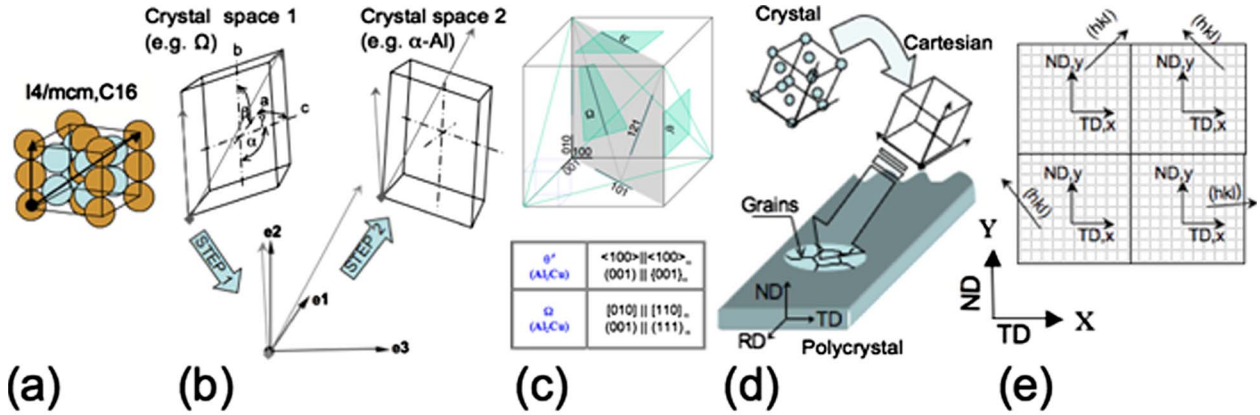

$$V_j^{elem} = T_{Poly}^{elem} T_{cart}^{Poly} M_{\alpha}^{cart} T_{\alpha^*}^{\alpha} M_{cart}^{\alpha^*} M_{\Omega}^{cart} V_j^{\Omega} \quad \text{(transforming } V_j^{\Omega} \text{ from the } \Omega \text{ crystal to element axes)}$$

$$V_j^{elem} = T_{Poly}^{elem} T_{cart}^{Poly} M_{\alpha}^{cart} V_j^{\alpha} \quad \text{(transforming } V_j^{\alpha} \text{ from the matrix crystal to element axes)}$$

Fig. 4 Illustration of slip vector (V_j) transformation sequence ((*a*)–(*e*)) to the element axes. (*a*) The slip system is identified in fractional coordinates. (*b*) The slip system vectors are transformed from precipitate space to matrix space. (*c*) The precipitate vectors are aligned with the matrix vectors in accordance with the orientation relationships. (*d*) The oriented slip vectors are mapped to the axes of the polycrystalline aggregate. (*e*) The vectors are mapped from the polycrystalline aggregate to the element axes.

$$\frac{d\rho_{im}^{(\alpha)}}{dt} = |\dot{\gamma}^{(\alpha)}| \left[\frac{g_{\text{minter}}}{B^{(\alpha)} B^{(\alpha)}} \exp\left(-\frac{\Delta H}{kT} \right) + \frac{g_{\text{immob}}}{B^{(\alpha)}} \sqrt{\rho_{im}^{(\alpha)}} - g_{\text{recov}} \exp\left(\frac{\Delta H}{kT} \right) \rho_{im}^{(\alpha)} \right] \tag{7}$$

where g_{sour}, g_{minter}, g_{recov}, and g_{immob} are coefficients corresponding to the generation of mobile dislocation densities, trapping of mobile dislocations by dislocation-dislocation interactions, rearrangement and annihilation of immobile dislocations by recovery, and immobilization of mobile dislocations, respectively. For a determination of these coefficients, see Ref. [21]. ΔH is the enthalpy of activation of plastic deformation, and k is the Boltzmann constant.

4.2 Precipitate-Crystal Representation. As seen from the Sec. 4.1, the crystal plasticity constitutive formulation requires the identification of the specific crystal structures, slip systems, and material properties. In Al–Cu alloys, the θ phase (Al_2Cu) has an $I4/mcm$ structure with $a=0.607$ nm and $c=0.487$ nm [22]. The θ' phase has a tetragonal structure $I\bar{4}m2$, with $a=0.404$ nm and $c=0.58$ nm [23]. The Ω phase (Al_2Cu) was proposed as monoclinic [24,25], hexagonal [26], and tetragonal distorted θ phases [27]. The accepted structure for the Ω phase was the orthorhombic structure ($Fmmm$) proposed by Knowles and Stobbs [28], with $a=0.496$ nm, $b=0.858$ nm, and $c=0.848$ nm. In this study, the Ω and θ' phases were modeled as $I4/mcm$ [27,29], using 12 slip systems corresponding to the shortest two Burgers vectors in the θ crystals ($C16$ structure) [30,31], and with the concomitant rational orientation relations to the matrix [22].

4.3 Orientation of Crystal Lattice With Respect to Element Axes. First, the Miller indices of planes and directions that define orientation relations between precipitates and matrix were defined. The following procedure was then used to crystallographically orient slip normals and directions within precipitates and the matrix with respect to the global axes, while observing matrix-precipitate orientation relations. A schematic representation of this procedure is shown in Fig. 4 along with the entire sequence of transformation matrices.

The slip directions and planes for the matrix and precipitates are defined in fractional coordinates. Since the precipitates are noncubic, the vectors defining slip-plane normals are not equivalent to their miller indices, and normals may be obtained by a reciprocal lattice construct. The vectors are then mapped from the precipitate space to the matrix space. This is achieved by the transformation sequence $[M_{\text{Cart}}^{\alpha*}][M_{\Omega}^{\text{Cart}}]$, where $[M_{\Omega}^{\text{Cart}}]$ transforms a vector in the precipitate (e.g., Ω) to a vector in a Cartesian frame, and $[M_{\text{Cart}}^{\alpha*}]$ takes the transformed vector from the Cartesian frame to the matrix crystal. The form of $[M]$ is adapted from Ref. [32]. The vectors are then aligned according to the orientation relations by matrix $[T_{\alpha*}^{\alpha}]$, followed by another transformation $[M_{\alpha}^{\text{Cart}}]$, taking vectors from the matrix space to a Cartesian space if necessary (i.e., matrix crystal is noncubic). Random Euler angles are then assigned to every grain to align crystal lattices, with respect to the polycrystalline aggregate axes. This transformation, defined as $[T_{\text{Cart}}^{\text{poly}}]$, is adapted from Ref. [33]. The polycrystalline aggregate axes are then aligned with the corotational frame of the element (initially identical to the drawing plane) using $[T_{\text{poly}}^{\text{elem}}]$.

4.4 Geometry of the Precipitate Crystals. A large aspect ratio ($L/t=24$) was chosen to be consistent with observed values in quaternary alloys [34]. Further, to capture a microstructural length scale consistent with precipitates, a thickness of 500 nm was used. Finally, a total volume fraction of 3% was assumed for the precipitates.

4.5 2D Finite Element Model. The multiple-slip dislocation-density based crystal plasticity formulation was implemented within the framework of the explicit dynamic FE program ABAQUS/EXPLICIT to investigate the behavior of a polycrystalline aggregate representative of 2139-Al under large compressive inelastic strains and strain rates. An 18 grain aggregate with dimensions of 100×100 μm^2 (Fig. 5) was used, where the grain size was of a maximum of 1000 μm^2. Random Euler angles were assigned for relative grain misorientations that did not exceed 10 deg. The Ω and θ' precipitates were placed near the centroid of each grain based on the crystallographic formulations as outlined earlier (i.e., having aligned their thickness and long directions in accordance with their rational orientation relationships, with re-

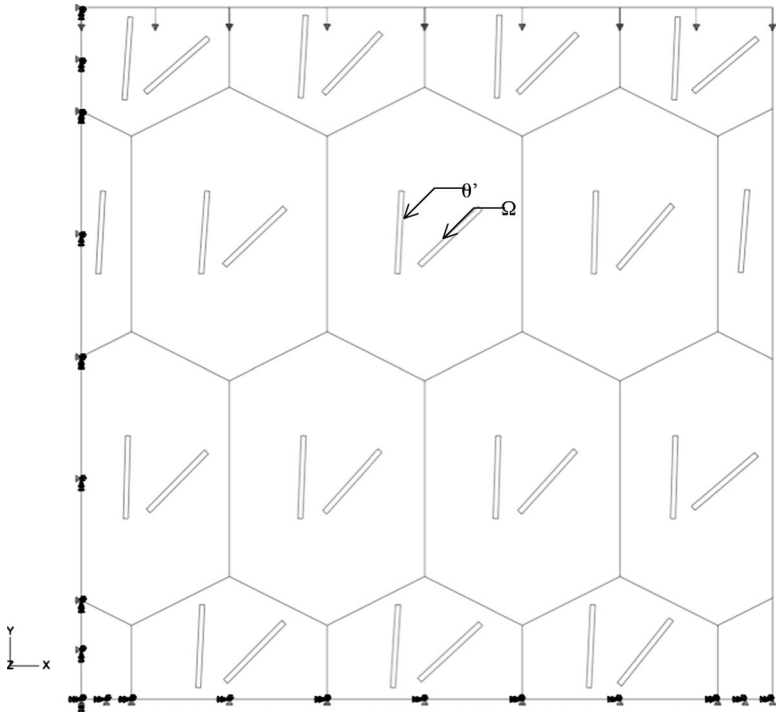

Fig. 5 An 18 grain aggregate with θ' and Ω precipitates, subject to an applied strain rate of 10^4 s^{-1} on the upper surface and with symmetry boundary conditions at the left and bottom edges

spect to each grain, and then projecting these directions in 2D). The material properties used in this study are summarized in Table 1 and accompanied by their respective references.

The aggregate was subjected to different nominal axial strain rates ranging from 10^{-3} s^{-1} to 10^4 s^{-1} by applying a velocity along the normal direction. Symmetry boundary conditions were applied for a 2D plane-strain deformation (Fig. 5) A convergent mesh of 6500 elements was used. Four-node bilinear plane-strain quadrilaterals, with one-point integration and enhanced assumed-strain hourglass control, were used. For representative behavior, the results for an applied strain rate of 10^4 s^{-1} will be presented in this paper.

5 Microstructural Finite Element Results

The contours of the accumulated plastic slip were shown in Fig. 6. The maximum accumulated plastic strain is 1.4 with most of the maximum accumulations occurring at the precipitate-matrix inter-

Table 1 Material properties for α-Al, Ω and θ'

Property	Description	Value		Reference
		Al	Ω, θ'	
E(GPa)	Young's modulus	69	140	[35]
ν	Poisson's ratio	0.34	0.34	
τ_y (MPa)	Static yield stress	35	35	—
ρ (g/cm^3)	Mass density	2.70	4.36	—
Cp (J/kg K)	Specific heat	902	902	[36]
$\Delta H/k$ (K)	Activation enthalpy/Boltzmann constant	2500	3100	[37]
$\dot{\gamma}_{\text{ref}}(s^{-1})$	Reference strain rate	0.001	0.001	[38]
$\dot{\gamma}_{\text{crit}}(s^{-1})$	Critical strain rate	10^4	10^4	
$\rho^0_{\text{im}}(m^{-2})$	Initial immobile dislocation density	10^{12}	10^8	—
$\rho^0_{\text{mo}}(m^{-2})$	Initial mobile dislocation density	10^{10}	10^6	—
T_0 (K)	Reference temperature	293	293	—
m	Strain rate sensitivity	0.02	0.02	[39]
ξ	Thermal softening exponent	0.5	0.5	
χ	Fraction of plastic dissipation to heat	0.9	0.9	
g_{source}	Dislocation source coefficient	2.76×10^{-5}	2.76×10^{-5}	[38]
g_{immob}	Dislocation immobilization coefficient	0.0127	0.0127	
g_{minter}	Mobile dislocation interaction coefficient	5.53	5.53	
g_{recov}	Recovery coefficient	6.69×10^5	6.69×10^5	
a_i	Slip-system interaction coefficient	0.5	0.5	

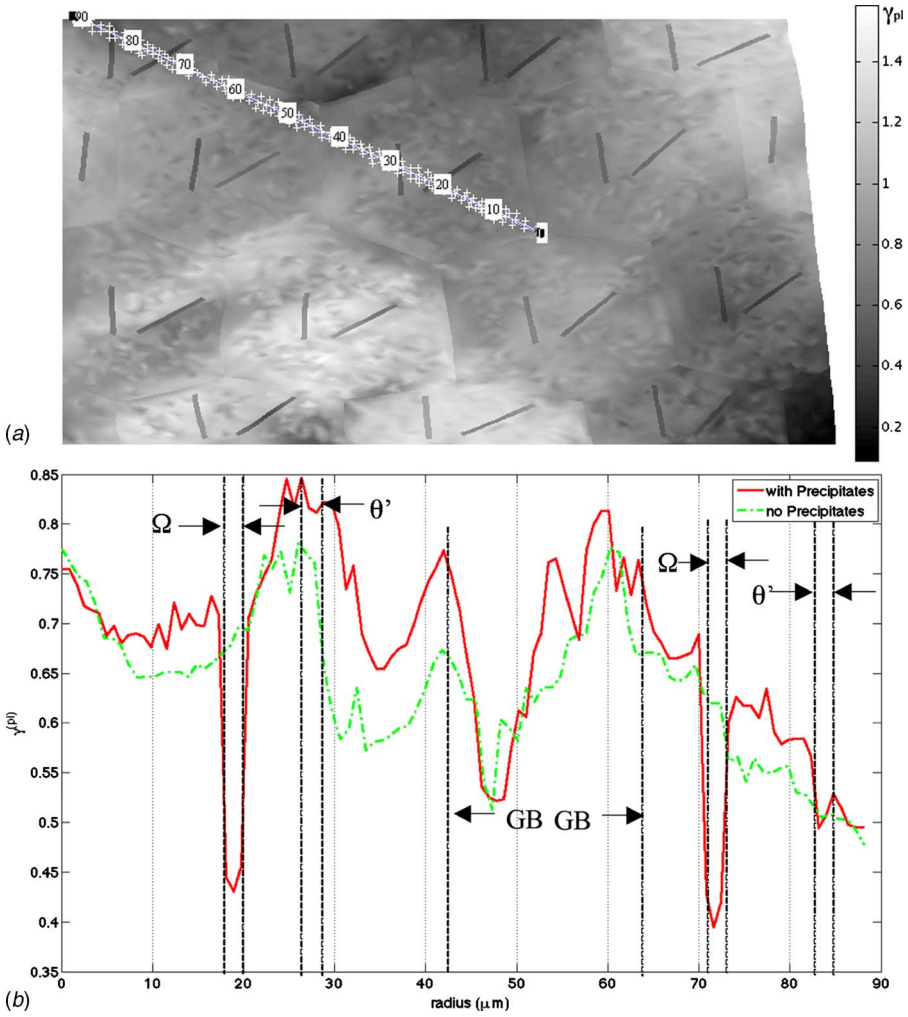

Fig. 6 (*a*) **Contour plot of plastic slip at a nominal strain of 25%.** (*b*) **Plastic slip comparison between 2139-Al and precipitate-free Al along path shown in** (*a*).

faces. The curves for the comparison between the precipitate-free aluminum and the 2139-Al indicate that the presence of precipitates has a significant effect on the plastic slip behavior and distribution. Specifically, the precipitates are clearly shear deformable. This is consistent with observations in Refs. [40–42]. The slip within the θ' and Ω precipitates has not resulted in slip concentration as was often observed with shearable particles [42–44]. This could be due to the precipitates continuing to harden and also acting as physical barriers that impede the matrix from forming large connected zones of intense plastic strain. Moreover, the FE model, though constrained in plane strain, showed plastic strain on multiple slip systems in the Ω and θ' precipitates. Therefore, slip in the precipitates was not planar, and shearing did not localize as would otherwise be expected [45].

The corresponding adiabatic temperature changes are shown in Fig. 7. The Ω precipitates along the selected evaluation path have a lesser increase in temperature than the θ' phase or the matrix, which indicates that these precipitates may delay thermal softening of the 2139-Al alloy. This, combined with the diffuse plastic slip accumulation, is another indication of 2139-Al's ductility and lack of susceptibility to shear-strain localization.

The contours in Fig. 8 show the immobile dislocation density corresponding to slip system $(111)[0\bar{1}1]$ in the matrix, which was the most active matrix system, and the immobile dislocation density corresponding to the most active system $(110)[\bar{1}12]$ for the precipitates. The contours indicate that the matrix slip system saturated to 10^{14} m^{-2} over most grains. This saturation actually occurred in most of the grains, at a nominal strain of approximately 12%, which was approximately equivalent to the true strain at which softening was first observed in the experimental stress-strain curves.

It was also seen that the dislocation densities attain maximum values at precipitate-free triple junction points and at precipitate-matrix interfaces. From the curve, it was seen that peaks in the immobile dislocation densities were at the matrix Ω interfaces. This accumulation at the precipitate interfaces further indicates the incompatibility of slip in the surrounding matrix with Ω precipitates, similar to the observations in Refs. [41,42,46] for $\{100\}_\alpha$ and $\{111\}_\alpha$ precipitates. This accumulation, however, does not occur for the θ' precipitates along the selected path. Furthermore, the largest immobile dislocation density for Ω precipitates was at 40% of the value in the matrix and θ', which have both saturated. This was therefore an indication that Ω precipitates can add further strength and ductility through the interrelated mechanism of material hardening and dislocation density generation.

The evolution of the reference shear stress values was shown in Fig. 9. It was clear from the contours that the Ω precipitates generally harden more than the surrounding matrix, and often more than the θ' precipitates. The curves in Fig. 9 show hardening peaks within the Ω precipitate well above those for the θ' precipitates or the matrix for the selected path. Hence, the Ω precipitates

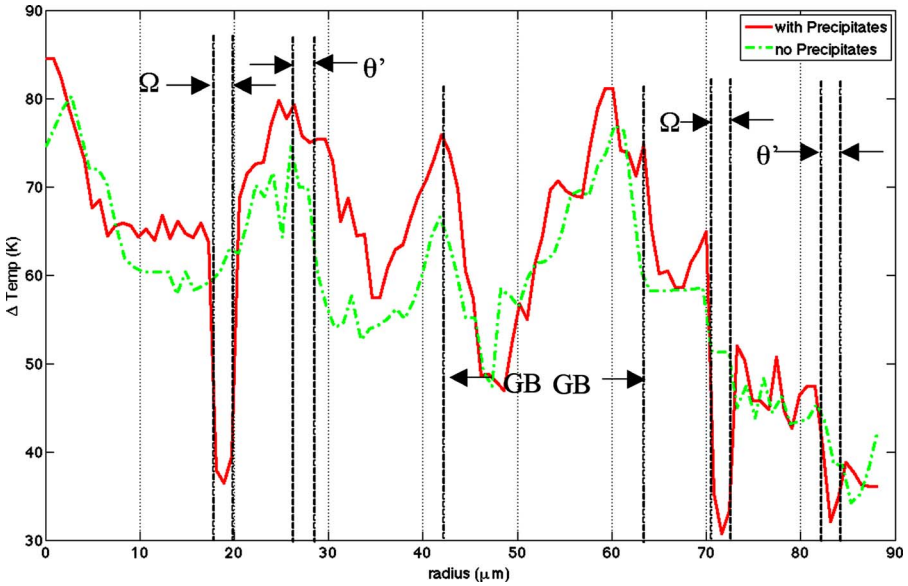

Fig. 7 Adiabatic temperature increase comparison between 2139-Al and precipitate-free Al along a selected path, showing the temperature build up to be the lowest inside the Ω precipitates

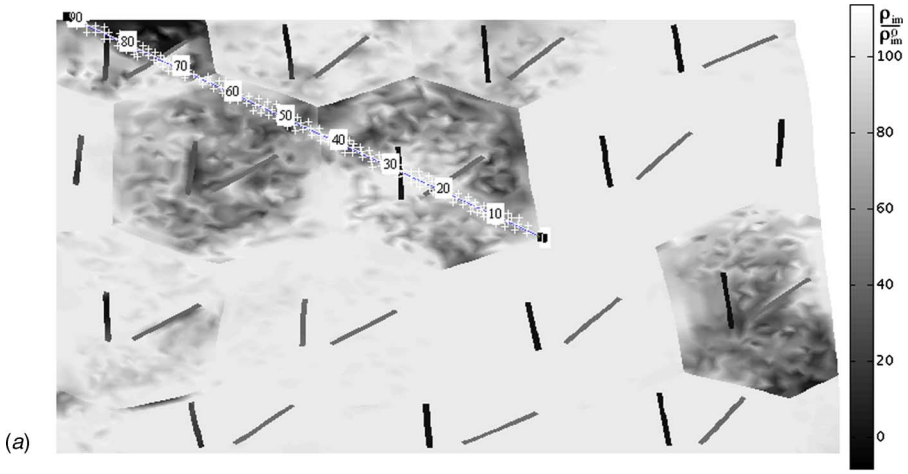

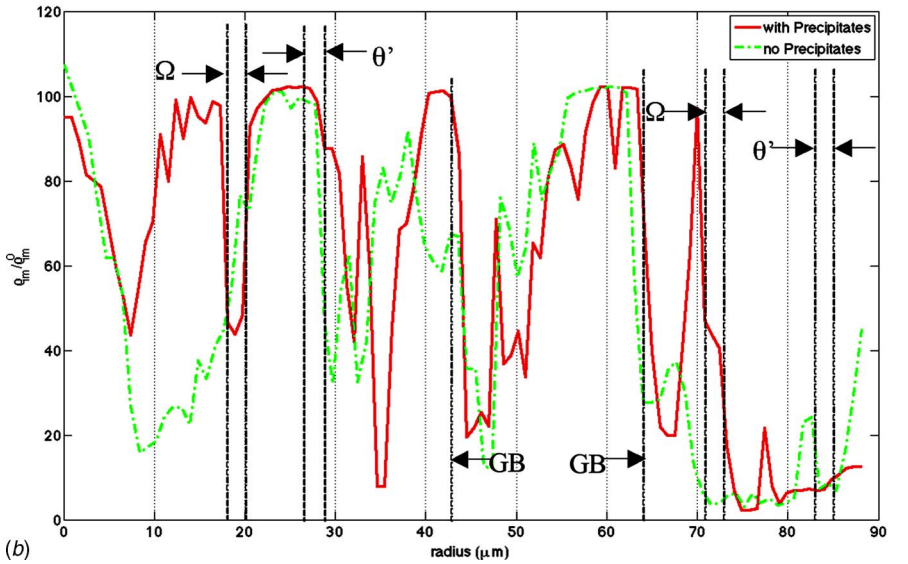

Fig. 8 (*a*) Contour plot of immobile dislocation density normalized by the initial density for (111)[$0\bar{1}1$] slip system in the matrix and (110)[$\bar{1}12$] in the precipitates at a nominal strain of 25% (i.e., most active slip systems). (*b*) Comparison of dislocation densities for most active slip systems between 2139-Al and precipitate-free Al along path shown in (*a*).

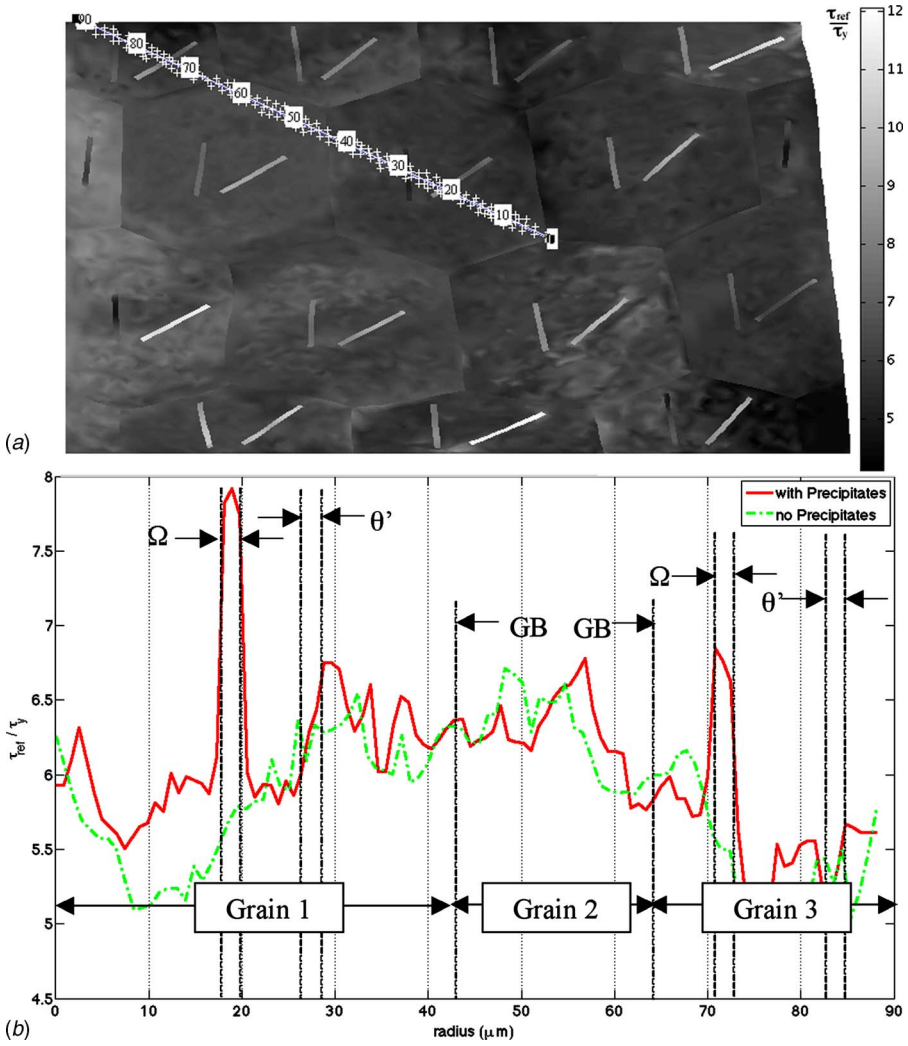

Fig. 9 (*a*) **Contour plot of reference shear stress normalized by static yield at a nominal strain of 25%.** (*b*) **Comparison of reference shear stress (normalized by static yield) between 2139-Al and precipitate-free Al along the path shown in** (*a*).

have a marked effect on strengthening the alloy, and it was more pronounced than that of the θ' precipitates. It was clear, however, that different grain orientations would align θ' and Ω differently, with respect to the loading direction, and could thus favor θ' hardening more than Ω. Hence, the effectiveness of precipitate strengthening of the alloy was dependent on the crystallographic orientation of the grains, which governs the relative precipitate orientations with respect to the loading of the aggregate, a dependence that was consistent with the observations and predictions in Refs. [46,47]. The presence, therefore, of both θ' and Ω, acting on different crystallographic orientations in the alloy, could be expected to enhance the strength and strain-hardening response [45] for the various grain orientations in the polycrystalline aggregate.

6 Summary

From the experiments, it was observed that the 2139-Al alloy exhibits considerable hardening at quasistatic strain rates ($\sim 10^{-3}$ s^{-1}), can be deformed to large equivalent strains, and has a strength of approximately 800 MPa, which was significantly higher than most aluminum alloys. As the strain rate was increased to 8100/s, 2139-Al exhibited significant ductility of up to 80%. There was slight stress softening, but the strengths were only slightly lower than those observed in the quasistatic regime. The stress-strain response softened in the dynamic regime at true strains of approximately 12%. Moreover, 2139-Al exhibits considerable rate sensitivity, particularly at strain rates beyond 10^3 s^{-1}. These results are an indication of 2139-Al's high strength, significant ductility, and lack of susceptibility to shear strain localization under compressive strain rates.

First principles calculations, describing the structure of the Ω-Al interface, indicated that the strongest bonding, and hence the greatest stabilization of the interface, occurs when the Mg substitutes for the Al layer closest to Ω phase, and the Ag substitutes for the Al in the next layer into the Al, hence forming an interfacial bilayer like that observed experimentally [16]. The theoretically determined structure allows strong Ag–Al, Mg–Cu and Ag–Mg bonding, while excluding the weaker Ag–Cu bonds. The analysis of the charge density at the interface showed a net transfer of electrons to the Ω and Al matrix from the interface region that contributes to interface stabilization. Hence, the first principles modeling provides both a viable atom-resolved structure consistent with experiment and an insight into the driving force for the stability of the Ω phase in terms of bonding strengths and electron charge transfer.

The predictions from the microstructural finite element model indicated that the precipitates continue to harden, and also act as physical barriers that impede the matrix from forming large connected zones of intense plastic strain. This understanding was

predicated on the accurate representation of the crystallography of the precipitates and the matrix. Moreover, the multiplicity of active slip systems resulted in the shearing of the precipitates, and this multiplicity also inhibited shear strain localization. As the predictions indicated, the combined effects of θ' and Ω, acting on different crystallographic orientations, enhance the strength and strain-hardening response of the alloy. The Ω precipitates had lower temperature increases than the matrix and therefore could delay thermal softening. Furthermore, dislocation densities in Ω have not saturated. Hence, Ω had the inherent capacity of increasing strength and ductility to the alloy through the interrelated mechanisms of hardening, and sustained ductility through precipitate shearing.

This integrated experimental and computational framework that spans different spatial and temporal scales provides a detailed understanding of the underlying mechanisms that delineate the high strength, ductility, and lack of susceptibility to shear strain localization of 2139-Al over a spectrum of dynamic compressive strain rates.

Acknowledgment

Support from the U.S. Army Research Office (Grant No. ARO W911 NF-06–1–0472) is gratefully acknowledged.

References

[1] Eschbach, L., Solenthaler, C., Uggowitzer, P. J., and Speidel, M. O., 1999, "Strength and Fracture Toughness of Spray Formed Al-Cu-Mg-Ag Alloys," Mater. Sci. Technol., **15**(8), pp. 926–932.

[2] Polmear, I. J., and Couper, M. J., 1988, "Design and Development of an Experimental Wrought Aluminium-Alloy for Use at Elevated-Temperatures," Metall. Trans. A, **19**(4), pp. 1027–1035.

[3] Hono, K., Sano, N., Babu, S. S., Okano, R., and Sakurai, T., 1993, "Atom Probe Study of the Precipitation Process in Al-Cu-Mg-Ag Alloys," Acta Metall. Mater., **41**(3), pp. 829–838.

[4] Howe, J. M., Basile, D. P., Prabhu, N., and Hatalis, M. K., 1988, "Minimum Detectable Solute Concentration in Atomic-Resolution Transmission Electron-Microscopy," Acta Crystallogr. A, **44**, pp. 449–461.

[5] Cho, A., and Bes, B., 2006, "Damage Tolerance Capability of an Al-Cu-Mg-Ag Alloy (2139)," Mater. Sci. Forum, **519–521**, pp. 603–608.

[6] Ma, J., Zikry, M., Ashamwi, W., and Brenner, D., 2007, "Hierarchical Modeling of Nanoindentation and Microstructural Evolution of Face-Centered Cubic Gold Aggregates," J. Mater. Res., **22**(3), pp. 627–643.

[7] Ortiz, M., Cuitino, A. M., Knap, J., and Koslowski, M., 2001, "Mixed Atomistic Continuum Models of Material Behavior: The Art of Transcending Atomistics and Informing Continua," MRS Bull., **26**(3), pp. 216–221.

[8] Kolsky, H., 1949, "An Investigation of the Mechanical Properties of Materials at Very High Rates of Loading," Proc. Phys. Soc. London, Sect. B, **62**, pp. 676–700.

[9] Lifshitz, J., and Leber, H., 1994, "Data-Processing in the Split Hopkinson Pressure Bar Tests," Int. J. Impact Eng., **15**(6), pp. 723–733.

[10] Kresse, G., and Hafner, J., 1993, "Ab Initio Molecular-Dynamics for Liquid-Metals," Phys. Rev. B, **47**(1), pp. 558–561.

[11] Kresse, G., and Hafner, J., 1994, "Ab-Initio Molecular-Dynamics Simulation of the Liquid-Metal Amorphous-Semiconductor Transition in Germanium," Phys. Rev. B, **49**(20), pp. 14251–14269.

[12] Perdew, J., Chevary, J. A., and Vosko, S. H., 1992, "Atoms, Molecules, Solids, and Surfaces-Applications of the Generalized Gradient Approximation for Exchange and Correlation," Phys. Rev. B, **46**(11), pp. 6671–6687.

[13] Vosko, S., Wilk, L., and Nusair, M., 1980, "Accurate Spin-Dependent Electron Liquid Correlation Energies for Local Spin-Density Calculations—A Critical Analysis," Can. J. Phys., **58**(8), pp. 1200–1211.

[14] Vanderbilt, D., 1990, "Soft Self-Consistent Pseudopotentials in a Generalized Eigenvalue Formalism," Phys. Rev. B, **41**(11), pp. 7892–7895.

[15] Monkhorst, H. J., and Pack, J. D., 1976, "Special Points for Brillouin-Zone Integrations," Phys. Rev. B, **13**(12), pp. 5188–5192.

[16] Hutchinson, C. R., Fan, X., Pennycook, S., and Shiflet, G., 2001, "On the Origin of the High Coarsening Resistance of ΩPlates in Al-Cu-Mg-Ag Alloys," Acta Mater., **49**, pp. 2827–2841.

[17] Orsini, V., and Zikry, M., 2001, "Void Growth and Interaction in Crystalline Materials," Int. J. Plast., **17**(10), pp. 1393–1417.

[18] Zikry, M. A., and Kao, M., 1996, "Inelastic Microstructural Failure Mechanisms in Crystalline Materials With High Angle Grain Boundaries," J. Mech. Phys. Solids, **44**(11), pp. 1765–1798.

[19] Ashmawi, W., and Zikry, M., 2002, "Prediction of Grain-Boundary Interfacial Mechanisms in Polycrystalline Materials," ASME J. Eng. Mater. Technol., **124**(1), pp. 88–96.

[20] Mughrabi, H., 1987, "A Tow Parameter Description of Heterogeneous Dislocation Distributions in Deformed Metal Crystals," Mater. Sci. Eng., **85**, pp. 15–31.

[21] Kameda, T., and Zikry, M. A., 1998, "Three Dimensional Dislocation-Based Crystalline Constitutive Formulation for Ordered Intermetallics," Scr. Mater., **38**(4), pp. 631–636.

[22] Wang, S. C., and Starink, M. J., 2005, "Precipitates and Intermetallic Phases in Precipitation Hardening Al-Cu-Mg-(Li) Based Alloys," Int. Mater. Rev., **50**, pp. 193–215.

[23] Silcock, J., Heal, T. J., and Hardy, H. K., 1955, "The Structural Ageing Characteristics of Ternary Aluminium-Copper Alloys With Cadmium, Indium or Tin," J. Inst. Met., **84**(1), pp. 23–31.

[24] Auld, J. H., 1972, "Structure of a Metastable Precipitate in an Al-Cu-Mg-Ag Alloy," Acta Crystallogr., Sect. A: Cryst. Phys., Diffr., Theor. Gen. Crystallogr., **28**, p. S98.

[25] Auld, J. H., 1986, "Structure of Metastable Precipitate in Al-Cu-Mg-Ag Alloys," Mater. Sci. Technol., **2**(8), pp. 784–787.

[26] Kerry, S., and Scott, V. D., 1984, "Structure and Orientation Relationship of Precipitates Formed in Al-Cu-Mg-Ag Alloys," Meat Sci., **18**(6), pp. 289–294.

[27] Garg, A., and Howe, J. M., 1991, "Convergent-Bean Electron-Diffraction Analysis of the Omega Phase in an Al-4.0 Cu-0.5 Mg-0.5 Ag Alloy," Acta Metall. Mater., **39**(8), pp. 1939–1946.

[28] Knowles, K. M., and Stobbs, W. M., 1988, "The Structure of (111) Age-Hardening Precipitates in Al-Cu-Mg-Ag Alloys," Acta Crystallogr., Sect. B: Struct. Sci., **44**, pp. 207–227.

[29] Ringer, S., and Hono, K., 2000, "Microstructural Evolution and Age Hardening in Aluminium Alloys: Atom Probe Field-Ion Microscopy and Transmission Electron Microscopy Studies," Mater. Charact., **44**(1–2), pp. 101–131.

[30] Bonnet, R., and Loubradou, M., 2002, "Crystalline Defects in a BCT Single Crystal Obtained by Unidirectional Solidification Along," Phys. Status Solidi A, **194**(1), pp. 173–191.

[31] Ignat, M., and Durand, F., 1976, "Deformation Lines on Al_2Cu Single Crystals After Creep in Compression," Scr. Metall., **10**(7), pp. 623–626.

[32] Giacovazzo, C., Monaco, H. L., Artioli, G., Viterbo, D., Ferraris, G., Gilli, G., Zanotti, G., and Catti, M., 2002, "Fundamentals of Crystallography," *IUCr Texts on Crystallography*, C. Giacovazzo, ed., Oxford University, New York, pp. 74–76.

[33] Randle, V., 1993, *The Measurement of Grain Boundary Geometry* (Electron Microscopy in Materials Science Series) Institute of Physics, Bristol, UK.

[34] Garg, A., Chang, Y. C., and Howe, J. M., 1990, "Precipitation of the Phase in an Al-4.0Cu-0.5Mg Alloy," Scr. Metall. Mater., **24**, pp. 677–680.

[35] Zhu, A. W., Shiflet, G. J., and Starke, E. A., 2006, "First Principles Calculations for Alloy Design of Moderate Temperature Age-Hardenable Al Alloys," Mater. Sci. Forum, **519–521**, pp. 35–43.

[36] Smithells, C. J., 2004, *Smithells Metals Reference Book*, Vol. 1, 8th ed., W. F., Gale, and T. C., Totemeier, eds., Elsevier, New York.

[37] Ali, A. A., Podus, G. N., and Sirenko, A. F., 1979, "Determining the Thermal Activation Parameters of Plastic Deformation of Metals From Data on the Kinetics of Creep and Relaxation of Mechanical Stresses," Strength Mater., **11**(5), pp. 496–500.

[38] Zikry, M., and Kao, M., 1997, "Inelastic Microstructural Failure Modes in Crystalline Materials: The S33A ANS S11 High Angle Grain Boundaries," Int. J. Plast., **13**(4), pp. 403–434.

[39] Zikry, M., 1994, "An Accurate and Stable Algorithm for High Strain-Rate Finite Strain Plasticity," Comput. Struct., **50**(3), pp. 337–350.

[40] Koda, S., Takahashi, S., and Matsuura, K., 1963, "Direct Observation of Interaction of Dislocations With W_{ij} Precipitates in an Aluminium-3.8 Wt.-Percent Copper Alloy," J. Inst. Met., **91**(7), pp. 229–234.

[41] Li, B. Q., and Wawner, F. E., 1998, "Dislocation Interaction With Semicoherent Precipitates ($[M^{\alpha*}_{\mathrm{Cart}}][M^{\mathrm{Cart}}_{\Omega}]$ Phase) in Deformed Al-Cu-Mg-Ag Alloy," Acta Mater., **46**(15), pp. 5483–5490.

[42] Nourbakhsh, S., and Nutting, J., 1980, "High-Strain Deformation of an Aluminium-4% Copper Alloy in the Supersaturated and Aged Conditions," Acta Metall., **28**(3), pp. 357–365.

[43] Polmear, I. J., 2006, *Light Alloys: From Traditional Alloys to Nanocrystals*, Elsevier/Butterworth-Heinemann, Burlington, MA, pp. 153–154.

[44] Sanders, T., and Starke, E. A., 1982, "The Effect of Slip Distribution on the Monotonic and Cyclic Ductility of Al-Li Binary-Alloys," Acta Metall., **30**(5), pp. 927–939.

[45] Polmear, I. J., 2006, *Light Alloys: From Traditional Alloys to Nanocrystals*, Elsevier/Butterworth-Heinemann, Burlington, MA, pp. 53–56.

[46] Nie, J. F., and Muddle, B. C., 2001, "On the Form of the Age-Hardening Response in High Strength Aluminium Alloys," Mater. Sci. Eng., A, **319–321**, pp. 448–451.

[47] Nie, J. F., Muddle, B. C., and Polmear, I. J., 1996, "The Effect of Precipitate Shape and Orientation on Dispersion Strengthening in High Strength Aluminum Alloys," Mater. Sci. Forum, **217–222**, pp. 1257–1263.